mild pressurization, which essentially eliminates the preclotting procedure. After implantation, tissue morphogenesis proceeded rapidly with time to regenerate vascular tissue close to the native one. Irrespective of the adipose connective tissue (39) or venous tissue fragments (37), tissue-sealed grafts were covered with thrombus in an early phase of implantation, and soon caused smooth neointimal tissue without any degenerative changes in a canine model. It is concluded that rapid endothelialization, followed by a high density of capillary network formation in the regenerated tissues, is due to the supply of a large amount of ECs migrating from fragmented tissues. This technique has been clinically applied without significant adverse effects (39).

Noishiki's more recent trial uses bone marrow, which is seeded in ePTFE prostheses (41,42). The transplanted bone marrow survived in the prostheses and accelerated neointimal formation on the luminal surface. A high level of bFGF secretion into a tissue was noted, which is a major contributor to neointimal tissue formation. No sign of differentiation of young primitive and highly proliferative cells in the bone marrow into vascular cell types was observed, indicating that bone marrow supplies a large amount of growth factor(s) which eventually recruit and proliferate ECs, but no "differentiation or transdifferentiation" of the cellular system occurred (42).

Although the tissue fragmentation method has been noted to be very effective for rapid tissue regeneration for medium- to large-diameter grafts, fragmented tissue-related thrombus formation, which occurs in the early phase of implantation, appears to be a major drawback when such a technique is applied to a small-diameter graft. The immersion of tissue-sealed graft into heparin solution appeared to help reduce the thrombus formation for a short time/ However, a more potent anticoagulation and long-lasting drug releasing system is necessary.

Tissue-engineered pulmonary artery

Small children suffering from congenital pulmonary artery diseases require age-dependent growable vascular prostheses which can enlarge with the children's growth. Shin'oka et al. devised a tissue-engineered device with biodegradable scaffold, poly(caprolactone-colactic acid) copolymer (weight ratio: 1 : 1) (43,44). Ten days after seeding of the mixture of vascular cell types, cells (ECs, SMCs and fibroblasts) were isolated from the patient's venous wall, and the grafts were autologously transplanted into the pulmonary artery. On follow-up angiography, the transplanted graft was noted to be completely patent. No evidence of graft occlusion or aneurismal changes on chest radiography were noted. Shin'oka et al. claimed that, in pediatric cardiovascular surgery, tissue engineering may play an important role as an alternative to transplantation and the use of an artificial graft. To date, more than a few tens of children have been successfully treated with Shin'oka's engineered tissues without any complications. Biodegradable polymers, which were designed to be degraded and adsorbed within eight months in the body, can constitute a temporary scaffold through which tissue ingrowth in vivo eventually replaces the prosthesis and leaves a complete biological vascular conduit. His revised procedure was to use bone marrow as a sobbing biologics? This eliminates the labor- and time-consuming procedure of cell harvesting and culturing in the former procedures.

Endothelial progenitor cell (EPC)

Recent studies have reported that a very small number of EPCs are circulating in the peripheral blood and they exhibit cell markers specific to ECs (45). The cloning of EPCs, achieved by the isolation of the mononuclear cell fraction of the whole blood and successive culturing on fibronectin-coated dishes in the medium enriched with VEGF, enabled EPCs to be the new cell source (46,47). The isolated EPCs, which were obtained at the average rate of approximately 18% of harvesting, were seeded on the collagen gel-coated microporous SPU grafts. EPC-covered grafts, autologously implanted into canine carotid arteries, produced neither thrombus nor intimal hyperplasia at three months after implantation. The smooth, glistening and ivory-colored luminal surfaces of implanted grafts was completely covered with cobblestone-like EPCs that secreted prostacycline as well as producing intracellular nitric oxide, both of which have potent antiplatelet activity. This finding indicates that EPCs are alternative luminal lining cells to ECs, thus ensuring non-thrombogenicity. The EPCs' harvesting is carried out by a minimally invasive procedure as compared with veins harvesting for ECs. However, the efficacy of harvesting was limited to approximately 20%, as mentioned above, and requires further improvement to attain the high efficacy of targeted cell harvesting which is needed for clinical application.

As an extension of the series of studies on EPC-based vascular tissue engineering, intraluminal EPC delivery systems were devised and tested in vitro and in vivo (48,49). The expandable stents, which were coated with cell adhesive photoreactive gelatin or wrapped with elastomeric microporous SPU film, were subjected to EPC seeding and subsequent cul-

turing. An EPC-innoculated, self-contracted collagen gel tube was also installed to cover the stents. Upon implantation and deployment of these stents in a vessel, EPCs were migrated from the inflated stent structs, hybrid tissues or microporous substrate and proliferated to form a confluent monolayer of EPC on the non-endothelialized diseased wall. This intraluminal EPC delivery and subsequent EPC "paving" technology on the vessel wall may introduce a new therapeutic procedure for the curing of injured or athelosclerotic sites in vascular walls.

Genetically-engineered fibroblasts

Since the difficulty of harvesting vascular cell types from patients hampers the use of vascular tissue-engineered grafts in clinical settings, an alternative cell source has long been awaited. Provisional or transient pseudoendothelial cells that secrete anticoagulant molecules and cytokines specifically enhance EC recruitment and proliferation. To this end, fibroblasts harvested from skin tissue were transfected by gene-encoding adenovirus to express various bioactive proteins, including a tissue factor pathway inhibitor (TFPI), which potently neutralize tissue factor (a very potent coagulation enzyme initiating the activation of an extrinsic pathway of the coagulation system) secreted from fibroblasts, C-type natriuretic peptide (CNP), which is a multipotent tissue modulator, and VEGF. This triple-gene-transfected, fibroblast-inoculated collagen gel wrapped with microporous SPU film was implanted into canine carotid arteries for up to three months postoperatively. In contrast to the result that all of the non-transfected fibroblast-inoculated grafts were occluded within two days after implantation, the three-gene-transfected fibroblast-based graft exhibited a high patency: 100% at one month and 70% at three months postoperatively. Thus, fibroblasts, which are very thrombogenic due to the secretion of TF, can be used as temporary or transient endothelial-like cells (50).

CONCLUSION

The search for small-diameter vascular graft substitute materials, biological modulators and fabrication process technologies to provide extracellular milieu in portions of diseased vessels similar to a natural physiological environment has a long history in artificial organs and biomaterials. Although seeking completely non-reactive substances to blood and the surrounding tissue is likely to be unrealistic, the incorporation of maximally-"passive" coatings as described here (Okano et al., Ishihara et al. and Kodama et al.) may elicit non-thrombogenic potential without the use of the natural non-thromobogenic liner, EC. The emergence of tissue-engineering technology has made the development of a novel biologically viable vascular substitute feasible (Noishiki et al., Matsuda et al. and Shin'oka et al.). When an appropriate cell sourcing, "mechano-active" and "tissue-permeable" scaffold design, and biologically active ECM or non-fouling coating are maximally incorporated into a designed small-diameter vascular graft, such a graft may be applicable in clinical settings. The mechano-biological, genetic and progenitor/stem cell engineering help to promote "real" vascular tissue morphogenesis. These disciplines and engineering, once combined, should give the ultimate solution for a long-awaited, functionally viable vascular substitute.

REFERENCES

1. Lian X, Howard PG. Biomaterial in the development and future of vascular grafts. *J Vasc Surg* 2003;37:472–80.
2. Nojiri C, Okano T, Koyanagi H, Nakahama S, Park KD, Kim SW. In vivo protein adsorption on polymers: visualization of adsorbed proteins on vascular implants in dogs. *J Biomater Sci* 1992;4:75–88.
3. Nojiri C, Nakahama S, Senshu K, et al. A newly amphiphilic block co-polymer with improved elastomeric properties for application in various medical devices. *ASAIO J* 1993;39:322–6.
4. Yoneyama T, Sugihara K, Ishihara K, Iwasaki Y, Nakabayashi N. The vascular prosthesis without pseudointima prepared by antithrombogenic phospholipid polymer. *Biomaterials* 2002; 23:145–9.
5. Yoneyama T, Ito M, Sugihara K, Ishihara K, Nakabayashi N. Small diameter vascular prosthesis with a nonthrombogenic phospholipid polymer surface: preliminary study of a new concept for functioning in the absence of pseudo- or neointima formation. *Artif Organs* 2000;24:23–8.
6. Wang C, Zhang Q, Uchida S, Kodama M. A new vascular prosthesis coated with polyamino-acid urethane copolymer (PAU) to enhance endothelialization. *J Biomed Mater Res* 2000;62:315–22.
7. Kito H, Matsuda T. Biocompatible coatings for luminal and outer surfaces of small-caliber artificial grafts. *J Biomed Mater Res* 1996;30:321–30.
8. Matsuda T, Sugawara T. Development of surface photochemical modification method for micropatterning of cultured cells. *J Biomed Mater Res* 1995;29:749–56.
9. Matsuda T, Sugawara T. Photochemical protein fixation on polyme surfaces via derivatized phenyl azido group. *Langmuir* 1995;11:2272–6.
10. Sugawara T, Matsuda T. Synthesis of phenylazido-derivatized substances and photochemical surface modification to immobilize functional groups. *J Biomed Mater Res* 1996;32:157–64.
11. Nakayama Y, Matsuda T. Surface macromolecular architectural designs using photo-graft copolymerization based on photochemistry of Benzyl N, N-diethyldithiocarbamate. *Macromolecules* 1996;29:8622–30.
12. Fry WJ, DeWeese MS, Kraft RO, Ernst CB. Importance of porosity in arterial prostheses. *Arch Surg* 1964;88:836–42.
13. White RA. The effect of porosity and biomaterial on the healing and long-term mechanical properties of vascular prostheses. *Trans Am Soc Artif Intern Org* 1988;34:95–100.

14. Hirabayashi K, Saitoh E, Ijima H, Takenawa T, Kodama M, Hori M. Influence of fibril length upon ePTFE graft healing and host modification of the implant. *J Biomed Mater Res* 1992;26:1433–47.
15. Hayashi K, Nakamura T. Material test system for the evaluation of mechanical properties of biomaterials. *J Biomed Mater Res* 1985;19:133–44.
16. Nakayama Y, Matsuda T. Surface microarchitectural design in biomedical applications: preparation of microporous polymer surfaces by excimer laser ablation technique. *J Biomed Mater Res* 1995;29:1295–301.
17. Matsuda T, Nakayama Y. Surface microarchitectural design in biomedical applications: in vitro transmural endothelialization on microporous segmented polyurethane films fabricated using an excimer laser. *J Biomed Mater Res* 1996;31:235–42.
18. Doi K, Nakayama Y, Matsuda T. Novel compliant and tissue-permeable microporous polyurethane vascular prosthesis fabricated using and excimer laser ablation technique. *J Biomed Mater Res* 1996;31:27–33.
19. Doi K, Matsuda T. Enhanced vascularization in a microporous polyurethane graft impregnated with basic fibrolast growth factor and heparin. *J Biomed Mater Res* 1997;34:361–70.
20. Masuda S, Doi K, Satoh S, Oka T, Matsuda T. Vascular endothelial growth factor enhances vascularization in microporous small caliber polyurethane grafts. *ASAIO J* 1997;43:M530–4.
21. Doi K, Matsuda T. Significance of porosity and compliance of microporous, polyurethane-based microarterial vessel on neoarterial wall regeneration. *J Biomed Mater Res* 1997;37: 573–84.
22. Sonoda H, Urayama S, Takamizawa K, Nakayama Y, Uyama C, Yasui H, Matsuda T. Compliant design of artificial graft: compliance determination by new digital X-ray imaging system-based method. *J Biomed Mater Res* 2002;60:191–5.
23. Sonoda H, Takamizawa K, Nakayama Y, Yasui H, Matsuda T. Coaxial double-tubular compliant arterial graft prosthesis: time-dependent morphogenesis and compliance changes after implantation. *J Biomed Mater Res* 2003;65A:170–81.
24. Weinberg CB, Bell E. A blood vessel model constructed from collagen and cultured vascular cells. *Science* 1986;231:397–400.
25. Miwa H, Matsuda T. An integrated approach to the design and engineering of hybrid arterial prostheses. *J Vasc Surg* 1994;19:658–67.
26. Matsuda T, Miwa H. A hybrid vascular model biomimicking the hierarchic structure of arterial wall: neointimal stability and neoarterial regeneration process. *J Thorc Cardiovasc Surg* 1995;110:988–97.
27. Ishibashi K, Matsuda T. Reconstruction of a hybrid vascular graft hierarchically layered with three cell types. *ASAIO J* 1994;40:M284–90.
28. He H, Matsuda T. Newly designed compliant hierarchic hybrid vascular graft wrapped with microprocessed elastomeric film (II) Morphogenesis and compliance change upon implantation. *Cell Transplant* 2002;11:75–87.
29. He H, Matsuda T. Arterial replacement with compliant hierarchic hybrid vascular graft: biomechanical adaptation & failure. *Tissue Eng* 2002;8:213–24.
30. Kanda K, Miwa H, Matsuda T. Phenotypic reversion of smooth muscle cells in hybrid vascular prostheses. *Cell Transplant* 1995;4:587–95.
31. Kanda K, Matsuda T. Behavior of arterial wall cells cultured on periodically stretched substrates. *Cell Transplant* 1993;2: 475–84.
32. Kanda K, Matsuda T. Mechanical stress-induced orientation and ultrastructural change of smooth muscle cells cultured in three-dimensional collagen lattices. *Cell Transplant* 1994;3: 481–92.
33. Kanda K, Matsuda T. In vitro reconstruction of hybrid arterial media with molecular and cellular orientation. *Cell Transplant* 1994;3:537–45.
34. Hirai J, Matsuda T. Self-organized, tubular hybrid vascular tissue composed of vascular cells and collagen for low-pressure-loaded venous system. *Cell Transplant* 1995;4:597–608.
35. Hirai J, Matsuda T. Venous reconstruction using hybrid vascular tissue composed of vascular cells and collagen: tissue regeneration process. *Cell Transplant* 1996;5:93–105.
36. Kobashi T, Matsuda T. Fabrication of compliant hybrid grafts supported with elastpmeric meshes. *Cell Transplant* 1999;8: 477–88.
37. Kobashi T, Matsuda T. Branched hybrid vessel: in vitro loaded hydrodynamic forces influence the tissue architecture. *Cell Transplant* 2000;9:93–105.
38. Noishiki Y, Tomizawa Y, Yamane Y. Effectiveness of fragmented autologous adipose tissue as a sealer of porous textile grafts: effect on endothelial development. *J Vasc Surg* 1994; 20:279–87.
39. Noishiki Y, Tomizawa Y, Yamane Y, Okoshi T, Satoh S, Matsumoto A. Acceleration of neointima formation in vascular prostheses by transplantation of autologous venous tissue fragments: application to small-diameter grafts. *J Thorac Cardiovasc Surg* 1993;105:796–804.
40. Matsumoto A, Noishiki Y, Ichikawa Y, Soma T, Kondo J, Kosuge T. Sealing of fabric vascular prosthesis with autologous adipose tissue—a preliminary report of its clinical application. *Artif Organs* 1995;19:51–6.
41. Noishiki Y. Bone marrow transplantation in vascular prostheses. *Mater Sci Eng* 1998;C6:227–33.
42. Noishiki Y, Tomizawa Y, Yamane Y, Matsumoto A. Autocrine angiogenic vascular prosthesis with bone marrow transplantation. *Nat Med* 1996;2:90.
43. Shin'oka T, Shum-Tim D, Ma PX, et al. Creation of viable pulmonary artery autografts through tissue engineering. *J Thorac Cardiovasc Surg* 1998;115:536–45: discussion 545–6.
44. Shin'oka T, Imai Y, Ikeda Y. Transplantation of a tissue-engineered pulmonary artery. *New Eng J Med* 2001;344:532–3.
45. He H, Shirota T, Yasui H, Matsuda T. Canine endothelial progenitor cell-lined hybrid vascular graft with nonthrombogenic potential. *J Thorc Cardiovasc Surg* 2003;126:455–64.
46. Shirota T, He H, Yasui H, Matsuda T. Human endothelial progenitor cell (EPC)-seeded hybrid graft: proliferative and antithrombogenic potentials of EPC. *Tissue Eng* 2003;9:127–36.
47. Shirota T, Yasui H, Shimokawa H, Matsuda T. Fabrication of endothelial progenitor cell (EPC)-seeded intravascular stent devices and in vitro endothelialization on hybrid vascular tissue. *Biomaterials* 2003;24:2295–302.
48. Shirota T, Yasui H, Matsuda T. Intraluminal tissue-engineered therapeutic stent using endothelial progenitor cell-inoculated hybrid tissue and in vitro performance. *Tissue Eng* 2003;9:473–85.
49. Asahara T, Murohara T, Sullvan A, Silver M, van der Zee R, Li T, Witzenbichler B, Schatteman G, Isner JM. Isolation of putative progenitor endothelial cells for angiogenesis. *Science* 1997;275:964–7.
50. He H, Kim K, Ueno M, Matsuda T. Genetically-engineered fibroblasts a temporary endothelial-like cells for vascular tissue engineering (in press).

Available online at www.sciencedirect.com
SCIENCE DIRECT
Biomaterials 25 (2004) 2859–2866
Biomaterials
www.elsevier.com/locate/biomaterials

A device for the spatio-regional delivery of a photocurable drug formulation

Hiromichi Sonoda[a,b], Hisataka Yasui[b], Takehisa Matsuda[b,*]

[a] Division of Cardiovascular Surgery, Graduate School of Medicine, Kyushu University, 3-1-1 Maidashi, Higashiku, Fukuoka 812-8582, Japan
[b] Division of Biomedical Engineering, Graduate School of Medicine, Kyushu University, 3-1-1 Maidashi, Higashiku, Fukuoka 812-8582, Japan

Received 23 June 2003; accepted 17 September 2003

Abstract

We devised a new transtissue drug-delivery system, based on a multiple-needle-arrayed injector that has 36 long and short needles on the needle head, to administer the drug into local points of the target tissue at a well-controlled depth and pitch. A preliminary in vitro study, focusing the time-dependent depth profiling of protein injected in agarose gel as a model tissue using confocal laser scanning microscope, was conducted to evaluate the performance of the multiple-needle-arrayed injector coupled with photoreactive gelatin (styrenated gelatin: St-gelatin) as the sustained-release vehicle. Rhodamine-conjugated albumin, which was mixed with the St-gelatin buffer solution, was the model drug of the in vitro study, and the mixture was injected into agarose gel using the multiple-needle-arrayed injector by single injection, followed by visible-light irradiation to photocure the gelatin solution. Time-dependent distribution from the injected material into the surrounding agarose gel was observed using a confocal laser scanning microscope up to seven days. Injection of the drug material and concomitant withdrawal of the syringe (termed multirod method) enabled the long- and short-rod-like injections into the agarose gel at the same locations of the injected sites. The model drug gradually diffused throughout the agarose gel. In an in vivo study, the comparison of the efficacy of the angiogenic protein (bFGF: 10 μg for each) with placebo was performed using the non-ischemic hind limb model of rabbits. Four weeks after injection, a significant increase in the number of angiogenic capillaries was observed in the mixed St-gelatin/bFGF group compared with that of placebo. The multiple-needle-arrayed injector coupled with a sustained-release vehicle may be an effective drug delivery system for realizing the spatio-regional distribution of angiogenic protein.

Keywords: Multiple-needle-arrayed injector; Drug delivery system; Styrenated gelatin

1. Introduction

Although therapeutic procedures aiming at systemic drug administration and concomitant local accumulation at diseased sites have been explored by modification of a drug or a designed drug carrier, the development of transtissue spatio-regional drug delivery technology, which enables direct delivery of a drug to a regionally targeted tissue at various depths, has been desired for particular diseases. One promising solution is the device-directed drug delivery system.

Therapeutic angiogenesis has recently received significant attention as an alternative procedure for patients who suffer from severely occlusive vascular diseases (e.g., arteriosclerosis obliterans and myocardial infarction) and also who failed the interventional angioplasty or revascularization. Therapeutic angiogenesis at a target tissue may be divided into three local delivery therapies, all of which are based on multiple injections using a single-needled syringe: protein [1–3], gene [4,5] and cell delivery [6,7]. Administration of angiogenic proteins (for example, basic fibroblast growth factor (bFGF), and vascular endothelial growth factor (VEGF), transgenics of angiogenic growth factors (for example, adenovirus encoding VEGF gene (AdVEGF), and naked plasmid DNA encoding VEGF gene (phVEGF), and cell transplantation (for example, endothelial progenitor cells and cardiomyocytes) have been experimentally and clinically attempted. However, there are potential problems involved in overcoming the shortcomings associated with these therapies.

*Corresponding author. Tel.: +81-92-642-6210; fax: +81-92-642-6212.
E-mail address: matsuda@med.kyushu-u.ac.jp (T. Matsuda).

0142-9612/$ - see front matter © 2003 Elsevier Ltd. All rights reserved.
doi:10.1016/j.biomaterials.2003.09.061

For the local administration of angiogenic proteins, a large dose and frequent administration are necessary, because the effective residence of low-molecular-weight proteins such as angiogenic proteins, which are localized at injected sites, should be very short, and high blood concentration due to angiogenic protein injection may induce the distribution of these mitogenic proteins in the whole body, resulting in potentially serious side effects, such as exacerbation of diabetic retinopathy or promotion of occult cancer [8–10]. As for gene therapy and cell transplantation, their efficacies have not yet been realized at a stable level. Furthermore, the administration of these substances or living cells has to be performed by local or multiple injections at various depths of a target tissue. This requires skillful techniques, and it may be difficult to control the dose of the injected drug and its spatial distribution including depth and pitch.

To solve these problems, we have developed a delivery device called the "multiple-needle-arrayed injector". This injector can administrate drugs into the tissue at different depths and regionally at multiple points of tissue by only a single injection. In addition, when the drug is mixed with visible-light-induced photopolymerizable gelatin, followed by injection and subsequent visible-light irradiation, the photocured gelatin serves as a drug carrier and reservoir, and thereby sustained release is feasible. In this article, we conducted pilot study demonstrating the effectiveness of the multiple-needle-arrayed injector coupled with the photoreactive gelatin as a drug-immobilizable biodegradable matrix, and demonstrate its therapeutic potential.

2. Materials and methods

2.1. Fabrication of injector

The multiple-needle-arrayed injector, which has short and long needles that are set alternately on the top face of the needle head, was custom-designed (Four Leaves Inc., Osaka, Japan; Fig. 1A). All parts of the injector were made of stainless steel (SUS 304). This injector, which is composed of a connector and a needle head with multiple needles, was designed to inject a drug- or cell-containing solution into tissues locally and multiply at different depths by a single injection.

Thirty-six (6 × 6) needles were arrayed on the top face of the needle head by insertion into the micropores of the top face (Figs. 1A and B). The outer and inner diameters of a needle were 0.4 and 0.3 mm, respectively, and the lengths of the short and long needles were 2.5 and 5.0 mm, respectively. The pitch between the needles was 2.0 mm. The needle head onto which the needles were set was connected with the screw-type connector (Fig. 1C). The bottom of the connector can be attached

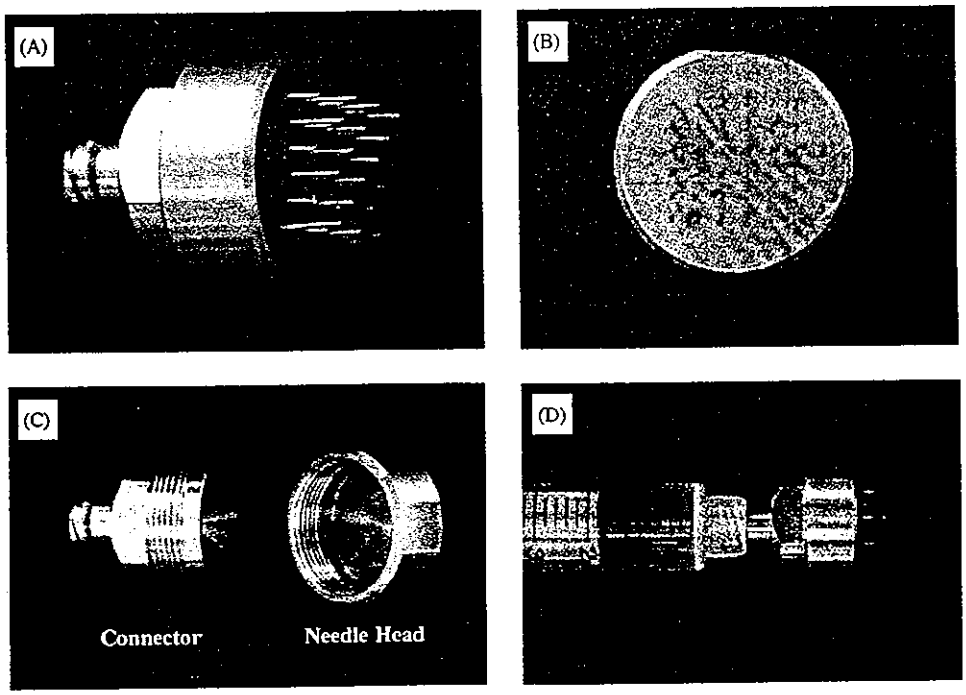

Fig. 1. External appearance of the multiple-needle-arrayed injector. (A) The intact injector. (B) Top view of the injector. (C) Separable needle head and connector. (D) Assembly of injector and syringe. Thirty-six (6 × 6) long (5.0 mm) and short (2.5 mm) needles were arrayed on the top face of the needle head. The needle outer diameter was 0.4 mm, and the pitch between needles was 2.0 mm. The needle head can be connected to a syringe using a screw-type connector.

to a syringe (Fig. 1D). Upon pushing the rod of the syringe, the drug solution in the syringe is first transported into the reservoir, which is an interspace between the connector and the needle head, and further pressing enables delivery of the solution through the multiple needles into the target tissue.

2.2. In vitro experiment

Rhodamine-conjugated albumin (molecular weight: 6.6×10^4, Sigma-Aldrich Co., Ltd., St. Louis, MO) was used as the model drug. Styrenated gelatin, which is in-house prepared photocurable gelatin and photocured in the presence of carboxylated camphorquinone (CQ) as the photocleavable radical generator under visible-light irradiation, was used as a sustained-release vehicle [11]. Detailed procedures including preparation of styrenated gelatin, photocuring characteristics and drug release characteristics were previously reported [12].

The in vitro pilot study was designed as follows: a mixed phosphate-buffered saline solution (PBS) (approximately 0.5 ml), which contained 0.125 wt% rhodamine-conjugated albumin, 30 wt% styrenated gelatin (28.9 styrene groups per gelatin molecule) and 0.05 wt% CQ, was used. The needles of the injector loaded with the mixed solution were inserted into 1.0 wt% agarose gel (Nacalai Tesque, Inc., Kyoto, Japan), and the model drug solution (approximately 0.5 ml) was slowly injected. Concomitantly, the needles were gradually removed from the gel. Visible-light irradiation of the drug-loaded gel was carried out for 3 min using an 80 W halogen lamp (Tokuso power lite, Tokuyama Co., Ltd., Tokuyama, Japan). Then, the agarose gel was immersed in PBS solution for up to seven days. Fluorescence images of the top views and the cross-sectional views of the agarose gel were observed using a confocal laser scanning microscope (CLSM: 543 nm excitation; Radiance 2000, Bio-Rad Laboratories, Inc., Hercules, CA) and fluorescence intensity of the rhodamine at various depths and regions was measured using a line-profile method.

2.3. In vivo experiment

Ten healthy Japanese white rabbits (average weight: 3.0 kg; range: 2.9–3.1 kg) were used in the in vivo experiment. The animal experiment was reviewed by the Committee on Ethics in Animal Experiments of Kyushu University Graduate School of Medical Sciences and was carried out in accordance with the Guideline for Animal Experiment at Kyushu University Graduate School of Medical Sciences and the Law (No. 105) and the Notification (No. 6) of the Japanese Government. The rabbits were anesthetized with an intravenous injection of xylazine (Celactal, Bayer AG, Leverkusen, Germany: 2.5 mg/kg) and ketamine (Ketaral 50, Sankyo Co., Ltd., Osaka, Japan: 30 mg/kg), and given intermittent injections of these anesthetics. Longitudinal skin incisions were bilaterally performed from inguinal ligament to just proximal portion of the patella, and bilateral thigh muscles were exposed. In total, 10 rabbits were used.

The injected materials (0.5 ml each) were divided into four groups ($n = 5$ for each) as follows:

(1) *Group I*: PBS (Placebo).
(2) *Group II*: 10 μg of recombinant human basic fibroblast growth factor (bFGF, R & D Systems, Inc., Minneapolis, MN) containing PBS (PBS + bFGF).
(3) *Group III*: 30 wt% styrenated gelatin (CQ: 0.05 wt%) solution (St-gelatin).
(4) *Group IV*: 10 μg of bFGF-containing 30 wt% styrenated gelatin (CQ: 0.05 wt%) solution (St-gelatin + bFGF).

After injection of these materials into the quadriceps muscle, four suture markings were performed using a 6-0 nylon suture 1 mm from the four corners of the injected site of the thigh muscle in order to identify the location of the injection at the second operation for extirpation of the thigh muscle. For Groups III and IV, visible light was irradiated to photocure the styrenated gelatin.

2.4. Arteriography

Four weeks after injection, all animals were anesthetized again and heparinized (Novo Heparin, Novo Nordisk Pharmaceuticals, Copenhagen, Denmark: 100 U/kg), and then femoral arteriography was performed with a single injection of contrast medium (Iomeron 350, Eisai Co., Ltd., Tokyo, Japan: 3 ml) via the abdominal aorta, with recording by the Toshiba cineangiography system (DG-15GB/CAS-CA, Toshiba Medical, Tokyo, Japan). After the arteriography, the animals were sacrificed by overdose anesthetics and the thigh muscles of animals from each group were removed and fixed with 10% formalin.

2.5. Histological examination

Three cross-sections (4 μm thick) each of all specimens were cut for observation at the middle, 3 mm proximal and distal portions of the nylon-marked harvested muscles, were histologically examined. For all hematoxylin-eosin stained samples, 10 randomly selected fields of each sample were subjected to determination of the capillary/muscle-fiber ratio under light microscopic observation ($\times 400$); the number of capillaries is divided by the total number of muscle fibers in the same field. In this study, the capillary is defined as the presence of the

luminal structure supported by endothelial-like cells and filled with red blood cells among the muscle fibers.

2.6. Statistical analysis

All capillary/muscle-fiber ratios are expressed as mean ± standard deviation. Statistical analysis was performed using one-way ANOVA followed by Tukey–Kramer's test. A P value of <0.05 was considered to be statistically significant.

3. Results

Using a newly designed and custom-fabricated multiple-needle-arrayed injector, protein injection was performed on agarose gel as model tissue. The depth profiling of injected protein and its time-dependent diffusion profile were determined by confocal laser scanning microscope (CLSM). Based on the results of in vitro pilot study, an in vivo study was conducted by injection of bFGF into rabbit quadrices muscle to assess the effective development of angiogenic capillaries.

3.1. Assembly of multiple-needle-arrayed injector and in vitro performance

The multiple-needle-arrayed injector (Fig. 1A) consisted of two parts: one is the needle head which has 36 short (height: 2.5 mm) and long (5.0 mm) needles which alternately installed with 2 mm of distance (Fig. 1B) between them, and the other is the screw-type connector (Fig. 1C). After assembly, the injector could be easily and tightly connected to a plastic syringe used clinically (Fig. 1D). The needle head was inserted into the model tissue (1.0 wt% agarose gel). As the injection of the model drug (rhodamine-conjugated albumin) solution proceeded with gradual pushing of the syringe rod, the needles were gradually removed from the agarose gel.

The CLSM technique was utilized to assess qualitatively and quantitatively the localization of the drug and its time-dependent permeation into the surrounding gel. Fig. 2 shows the fluorescence images of the top views and the fluorescence intensities of the scanning region immediately after photoirradiation, one and seven days after injection. Fig. 3 shows the fluorescence images of the cross sections and the fluorescence intensities of the scanned region. Top views show that the fluorescence images of the injected rhodamine-conjugated albumin were observed; a regular array was observed with many "spot-like" circular or irregular elliptical shapes at the same locations as the injected sites (Figs. 2A–C). Immediately after the injection, high-intensity fluorescent regions surrounded by diffused regions existed (Fig. 2A). Depth profiling of the fluorescence intensity showed periodic large peaks with high intensity and relatively large width (Fig. 2D). Even the lowest fluorescence intensity observed at the valley between two adjacent peaks was relatively high. These results suggest that the drug spontaneously diffuses into the surrounding gel after injection. The cross-sectional view shows that the drug was localized at a rod-like region,

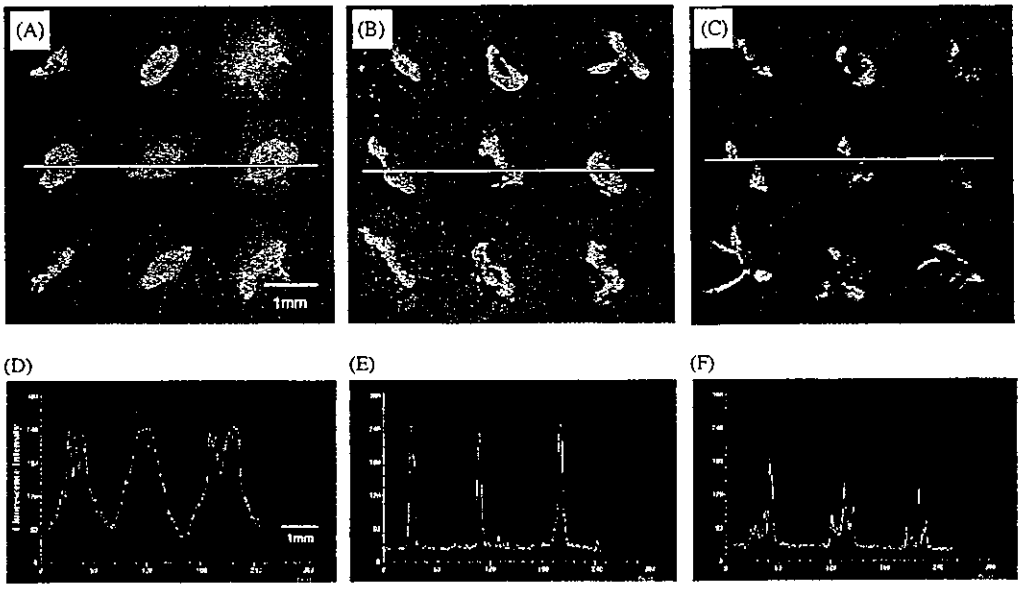

Fig. 2. Top views of confocal laser scanning microscopic images after injection of photocurable styrenated gelatin solution mixed with rhodamine-conjugated albumin into agarose gel using the multiple needle-arrayed injector. Upper micrographs show fluorescence images taken immediately after photoirradiation (A), and one day (B), and seven days (C) after immersion in PBS. Lower graphs show the relationship between fluorescence intensity and distance of the line-scanning region (yellow lines in upper micrographs) of the above fluorescence images taken immediately after photoirradiation (D), and one day (E) and seven days (F) after immersion in PBS.

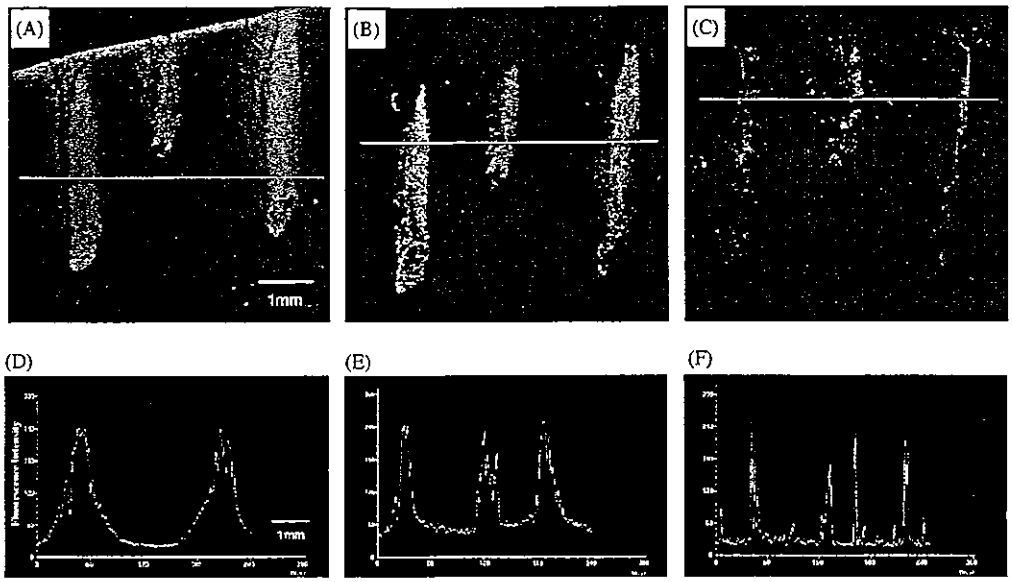

Fig. 3. Cross-sectional views of confocal laser scanning microscopic images after injection of the photocurable styrenated gelatin solution mixed with rhodamine-conjugated albumin into agarose gel using the multiple-needle-arrayed injector. Upper micrographs show fluorescence images taken immediately after photoirradiation (A), 1 day (B), and 7 days (C) after immersion in PBS. Lower graphs show the relationship between fluorescence intensity and distance of the line-scanning region (yellow lines in upper micrographs) of the above fluorescence images taken immediately after photoirradiation (D), 1 day (E), and 7 days (F) after immersion in PBS.

and localization of the drug clearly differed depending on the needle length (Figs. 3A–C). The measured length of the rod-like region was approximately 4.5 mm for the long one, and 2.2 mm for the short one, both of which are very similar to the respective lengths of the needles.

At 1 day after the injection of the drug, although the peak intensity was the same as that immediately after photoirradiation the peak width became small (Figs. 2E and 3E). At 7 days after injection, in both top and cross-sectional views, the peak intensity at the injected sites was markedly decreased, and the peak width became even smaller (Figs. 2F and 3F).

3.2. *In vivo experiments*

After an injector-driven injection was applied to rabbit quadriceps muscle, microarteriography and histochemical staining were performed to assess the development of angiogenic capillaries four weeks after the injection. Fig. 4 shows representative arteriographic photos taken from the four groups: Group I (PBS; control or placebo, Fig. 4A), Group II (PBS + bFGF, Fig. 4B), Group III (St-gelatin; control, Fig. 4D) and Group IV (St-gelatin + bFGF, Fig. 4C). Although there is no significant difference in the degree of angiogenesis among these groups, the number of capillaries for Group IV (St-gelatin + bFGF) appears to be higher than those of the other three groups (Fig. 4C).

Hematoxylin-eosin staining of tissue shows, capillaries observed in the muscle fibers as exemplifed in Fig. 5. Fig. 6 shows capillary/muscle-fiber ratios of the

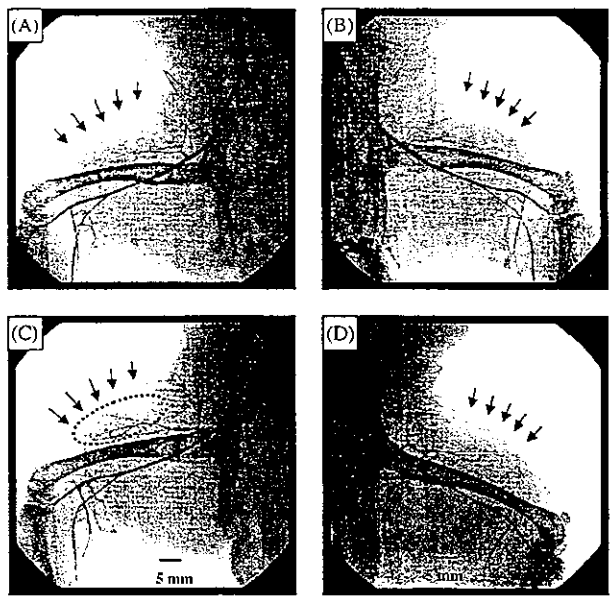

Fig. 4. Arteriographic findings. (A) PBS group (Group I), (B) PBS + bFGF group (Group II), (C) styrenated gelatin + bFGF group (Group IV) and (D) styrenated gelatin group (Group III). Arrows indicate the injection areas. The dotted circle indicates the area where increased angiogenesis was observed in Group IV.

quadriceps muscle of four groups. The capillary/muscle-fiber ratio (given as a percentage) of Group II (PBS + bFGF) was significantly higher than that of Group I (PBS: placebo) ($6.5 \pm 3.2\%$ vs. $4.1 \pm 2.1\%$, $P < 0.05$). The capillary/muscle-fiber ratio of Group IV (St-gelatin + bFGF) was significantly higher than that of

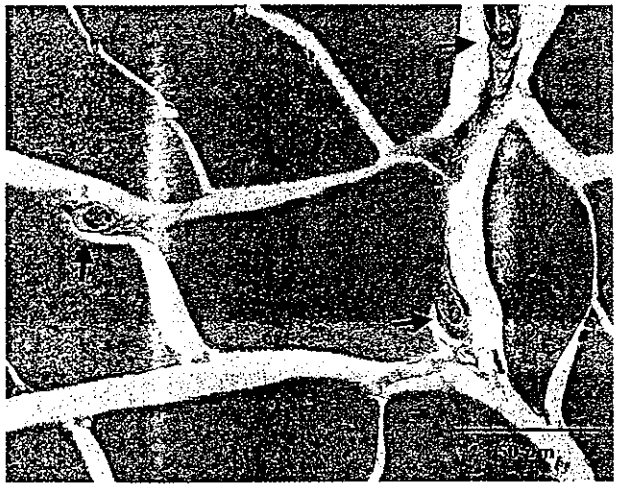

Fig. 5. Microscopic view of the cross section of the quadriceps muscle at four weeks after injection (hematoxylin-eosin staining). Arrows indicate capillaries.

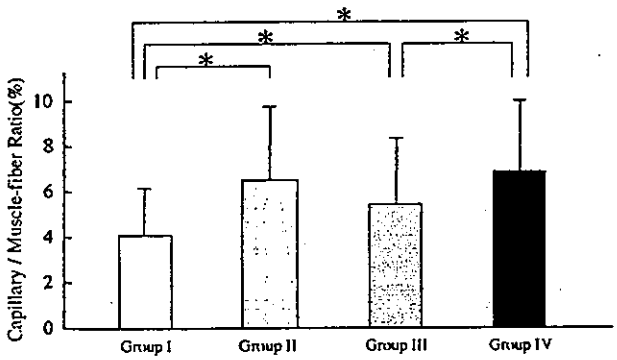

Fig. 6. Capillary/muscle-fiber ratios after injection. Group I: PBS; control group, Group II: PBS+bFGF group, Group III: styrenated gelatin group, and Group IV: styrenated gelatin+bFGF group. *: $P<0.05$.

Group III (St-gelatin: control) ($6.8\pm3.2\%$ vs. $5.4\pm2.9\%$, $P<0.05$). Furthermore, the capillary/muscle-fiber ratio of Group III was significantly higher than that of Group I ($5.4\pm2.9\%$ vs. $4.1\pm2.1\%$, $P<0.05$). However, there is no statistically significant difference in the capillary/muscle-fiber ratio between Group II and Group IV ($P=0.37$).

It is of interest to examine the fate of the photocured gelatin. As can be seen in Fig. 7, a long small-diameter photocured gelatinous rod existed among muscle fibers, which started from the inlet site of the tissue to a deep region that was approximately 5 mm from the inlet. This length corresponds to that of long needles. It is apparent that photocured gelatin was being biodegraded and sorbed away, leaving foam-like organized tissue. Since the number of recruited inflammatory cells was small, inflammatory reaction was found to be very mild.

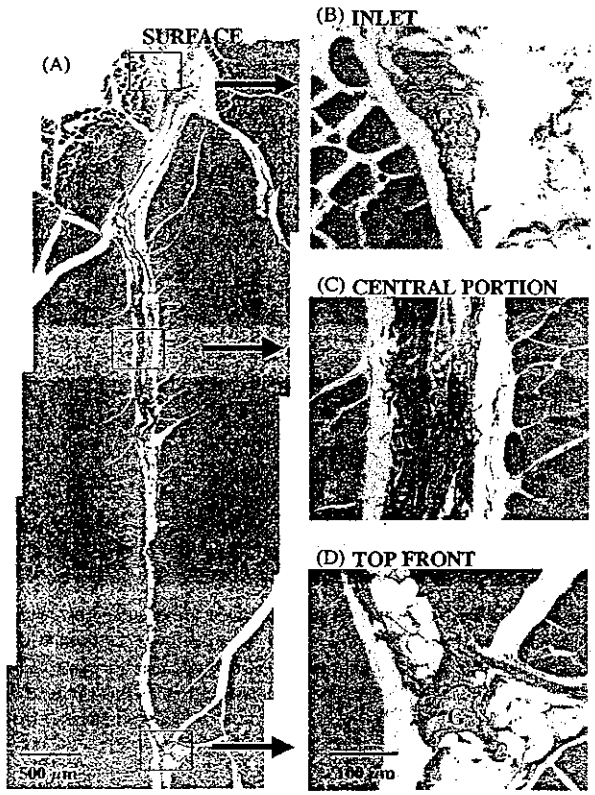

Fig. 7. Histological findings of the injected photocured gelatin four weeks after injection. (A) Gross finding at low magnification (original magnification: ×40). (B) Inlet site of the injected gelatin, (C) central portion of the injected gelatin, and (D) top front of the injected gelatin at high magnification (original magnification: ×200). G: injected photocured gelatin.

4. Discussion

Recently, therapeutic angiogenesis has been considered as a new treatment regimen for drug-refractory ischemic diseases to salvage ischemic lesions that cannot be cured by conventional angioplasty or bypass grafting. This treatment includes the administration of angiogenic proteins by systemic or local injection [1–3], gene transfection [4,5] and cell transplantation [6,7]. The angiogenic potential of angiogenic proteins has been demonstrated in in vivo studies using ischemic models [1,2]. However, the optimum dose of angiogenic proteins, the duration of pharmacological effect and the method of administration have not been standardized yet. Since the residence time of the angiogenic proteins at injected sites should be short, and low molecular weight proteins circulating in blood are usually metabolized within a short time, it may be necessary to administer them in large and repeated doses in order to maintain the effective concentration in ischemic lesions. However, high doses of angiogenic proteins may have adverse effects such as exacerbation of diabetic retinopathy or promotion of occult cancer,

and may also be expensive. Therefore, if the sustained release of angiogenic protein can be realized locally in the target ischemic tissue at a dose lower than that leading to side effects, the angiogenesis can be induced more effectively, and safely, and at a lower cost.

The methods for administering drug coupled with a sustained release vehicle are divided into three (Fig. 8). The first one, which is called the one-point injection method, involves single injection using only one needle (Fig. 8A). Here, the injected drug will be distributed only near the injected site. The second method, called the multipoint-injection method, involves multipoint injection using a multiple-needle-arrayed injector without gradual removal of the injector's needles from the tissue (Fig. 8B). In this case, locally and multiply injected drug can be distributed widely over a certain region compared with the first method. The third method, called the multi-rod method, involves rod-like injection as shown in Fig. 8C. Concomitant drug injection and syringe withdrawal can take place in this rod-like injection. This method can distribute the drug into the widest region at various depths by changing the length and pitch of the needles.

In this study, we developed a prototype of the multiple-needle-arrayed injector and evaluated the in vitro and in vivo performances of a local delivery system that uses this injector with styrenated gelatin as the sustained-release vehicle. In addition, the multiple-needle-arrayed injector was able to perform controlled and multiple injections spatio-regionally at various depths and widths.

Regarding the design of the multiple-needle-arrayed injector, 36 needles were set within a 1 cm^2 area (needle diameter: 0.4 mm) and long and short needles (lengths: 5.0 and 2.5 mm, respectively) were used in this study. Because the needle density, pitch, length and diameter can be changed, the design of the multiple-needle-arrayed injector can be adapted to the purpose of injection (such as higher density with thinner needles).

The in vitro experiment using agarose gel as model tissue showed that the injection of the model drug (rhodamine-conjugated albumin) coupled with styrenated gelatin and CQ was possible using the multi-rod method, and that long- and short-rod-like drug reservoirs could be realized. Studies of the time-dependent changes up to 7 days showed that the gradual distribution of the model drug from the vehicle into the surrounding model tissue was observed. The sustained-release rate of the drug from photocured gelatin may be controlled by manipulating the photocuring characteristics by changing the concentration of the styrenated gelatin and CQ. The study on detail manipulation of releasing rate from photocured gelatin was already reported in our previous article [12].

On the other hand, the in vivo pilot experiment using non-ischemic rabbit hind-limb muscles showed that the injection of a small amount of angiogenic protein (10 μg of bFGF) induced neovascularization around the injected site, but did not show that application of the

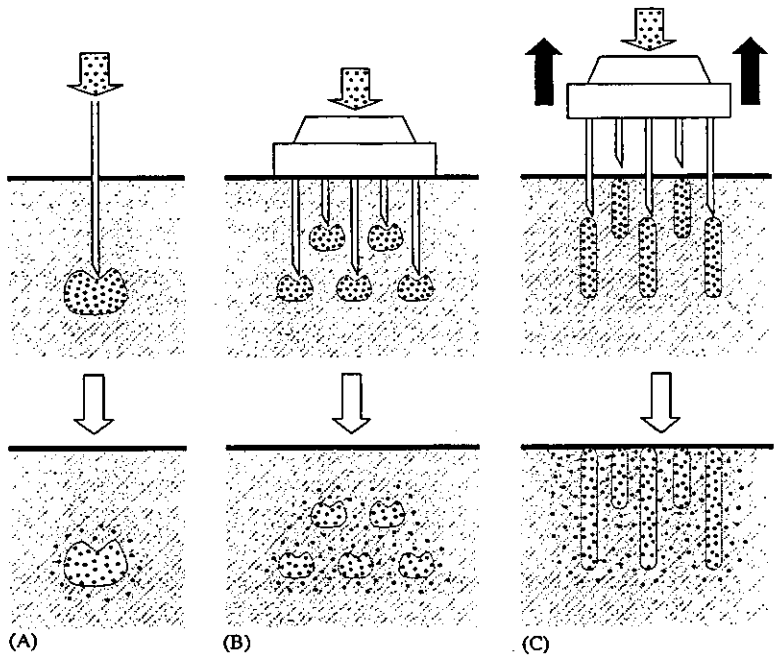

Fig. 8. Methods for administering drug into tissue coupled with the sustained release vehicle. (A) Single injection using only one needle (one-point injection method). (B) Multipoint injection using multiple-needle-arrayed injector without gradual removal of injector's needles from tissue (multipoint injection method). (C) Rodlike injection using multiple-needle-arrayed injector with gradual removal of injector's needles from tissue (multi-rod method).

sustained release of bFGF (Group IV: St-gelatin+ bFGF) was more effective than that of the bFGF solution (Group II: PBS+bFGF), as verified by histological examination. Although the styrenated gelatin remained within the injected site four weeks after injection (Fig. 7), further systematic research is necessary to provide strong evidence of the efficacy of the sustained-release method with ischemic tissues.

This pilot study aimed at evaluating the potential of the multiple-needle-arrayed injector coupled with visible-light-photocured gelatin as a sustained vehicle, and demonstrated the ease of handling and the prolonged spatio-regional drug distribution. More detailed investigation is necessary to reveal the potential of the multipoint and rodlike injection as a sustained-release model. We surmise that device-directed transtissue or the transdermal delivery system, exemplified in this study, promise superior potential of spatio-regional pharmacological effectiveness, cost-effective performance and markedly reduced the systemic side effects.

Acknowledgements

This study was financially supported in part by the Promotion Fundamental Studies in Health Science of the Organization for Pharmaceutical Safety and Research (OPSR) under Grant No. 97-15, and by Grants-in-Aid for Scientific Research (A2-12358017, B2-12470277) from the Ministry of Education, Culture, Sports, Science and Technology of Japan.

References

[1] Leung DW, Cachianes G, Kuang WJ, Goeddel DV, Ferrara N. Vascular endothelial growth factor is a secreted angiogenic mitogen. Science 1989;246:1306–9.

[2] Unger EF, Banai S, Shou M, Lazarous DF, Jaklitsch MT, Scheinowitz M, Correa R, Klingbeil C, Epstein SE. Basic fibroblast growth factor enhances myocardial collateral flow in a canine model. Am J Physiol 1994;266:H1588–95.

[3] Walder CE, Errett CJ, Bunting S, Lindquist P, Ogez JR, Heinsohn HG, Ferrara N, Thomas GR. Vascular endothelial growth factor augments muscle blood flow and function in a rabbit model of chronic hindlimb ischemia. J Cardiovasc Pharmacol 1996;27:91–8.

[4] Schwarz ER, Speakman MT, Patterson M, Hale SS, Isner JM, Kedes LH, Kloner RA. Evaluation of the effects of intramyocardial injection of DNA expressing vascular endothelial growth factor (VEGF) in a myocardial infarction model in the rat-angiogenesis and angioma formation. J Am Coll Cardiol 2000;35:1323–30.

[5] Mack CA, Patel SR, Schwarz EA, Zanzonico P, Hahn RT, Ilercil A, Devereux RB, Goldsmith SJ, Christian TF, Sanborn TA, Kovesdi I, Hackett N, Isom OW, Crystal RG, Rosengart TK. Biologic bypass with the use of adenovirus-mediated gene transfer of the complementary deoxyribonucleic acid for vascular endothelial growth factor 121 improves myocardial perfusion and function in the ischemic porcine heart. J Thorac Cardiovasc Surg 1998;115:168–76.

[6] Asahara T, Murohara T, Sullivan A, Silver M, van der Zee R, Li T, Witzenbichler B, Schatteman G, Isner JM. Isolation of putative progenitor endothelial cells for angiogenesis. Science 1997;275:964–7.

[7] Kamihata H, Matsubara H, Nishiue T, Fujiyama S, Tsutsumi Y, Ozono R, Masaki H, Mori Y, Iba O, Tateishi E, Kosaki A, Shintani S, Murohara T, Imaizumi T, Iwasaka T. Implantation of bone marrow mononuclear cells into ischemic myocardium enhances collateral perfusion and regional function via side supply of angioblasts, angiogenic ligands, and cytokines. Circulation 2001;104:1046–52.

[8] Gilbert RE, Vranes D, Berka JL, Kelly DJ, Cox A, Wu LL, Stacker SA, Cooper ME. Vascular endothelial growth factor and its receptors in control and diabetic rat eyes. Lab Invest 1998;78:1017–27.

[9] Ozaki H, Seo MS, Ozaki K, Yamada H, Yamada E, Okamoto N, Hofmann F, Wood JM, Campochiaro PA. Blockade of vascular endothelial cell growth factor receptor signaling is sufficient to completely prevent retinal neovascularization. Am J Pathol 2000;156:697–707.

[10] Gross JL, Herblin WF, Dusak BA, Czerniak P, Diamond MD, Sun T, Eidsvoog K, Dexter DL, Yayon A. Effects of modulation of basic fibroblast growth factor on tumor growth in vivo. J Natl Cancer Inst 1993;85:121–31.

[11] Nakayama Y, Matsuda T. Photocurable surgical tissue adhesive glues composed of photoreactive gelatin and poly(ethylene glycol) diacrylate. J Biomed Mater Res 1999;48:511–21.

[12] Okino H, Nakayama Y, Tanaka M, Matsuda T. In situ hydrogelation of photocurable gelatin and drug release. J Biomed Mater Res 2002;59:233–45.

Substrate-dependent cellular behavior of Swiss 3T3 fibroblasts and activation of Rho family during adhesion and spreading processes

Shinya Kato, Satoru Kidoaki, Takehisa Matsuda
Division of Biomedical Engineering, Graduate School of Medicine, Kyushu University, Maidashi 3-1-1, Higashi-ku, Fukuoka 812-8582, Japan

Received 29 August 2002; revised 24 June 2003; accepted 24 July 2003
Published online 18 December 2003 in Wiley InterScience (www.interscience.wiley.com). DOI: 10.1002/jbm.a.20012

Abstract: Recent biochemical studies revealed that intracellular Rho guanosine triphosphatases (Rho, Rac1, and Cdc42) are key regulatory molecules that link surface receptors to cytoskeletal organization and regulation of cell shape/morphology/motility. In this study, Swiss 3T3 fibroblasts were cultured on three representative substrates [tissue culture polystyrene dishes, nontreated polystyrene, and poly(ethylene terephthalate)] for 24 h after plating. Time-dependent changes in cell shape, morphology, cytoskeletal dynamics, and motility as well as Rho family activities were determined on each substrate. The cells on tissue culture polystyrene and on poly(ethylene terephthalate), which induced rapid and relatively rapid cell spreading, respectively, expressed Rac1 and Cdc42 activities continuously during the observation period. In contrast, such activities were suppressed in cells on polystyrene, which induced slow spreading but the highest cell motility compared with the other two substrates. Although a clear-cut relationship between cellular behavior and Rho family activation was not obtained, substrate-dependent coordinated control of cellular activities by Rho family is discussed. © 2003 Wiley Periodicals, Inc. J Biomed Mater Res 68A: 314–324, 2004

Key words: Rho family; cell shape; cell morphology; cytoskeletal organization; cell motility

INTRODUCTION

Tissue morphogenesis, the control of which is essential for the construction of functional vital engineered tissues,[1–4] is driven by spatio-temporally coordinated changes in cell shape, growth, and motility. Such complex biological processes, which also determine wound healing and cellular homeostasis in two- or three-dimensional extracellular milieu, require precise control of cellular behaviors including adhesion, spreading, proliferation, and migration. This is achieved by stimuli from the extracellular milieu, which is conducted by the collaborative effects of both soluble regulatory molecules such as cytokines and extracellular macromolecules such as adhesive proteins including collagen and fibronectin. Upon adhesion on extracellular macromolecules, cells, which are round in suspension, initiate spreading with time. Major intracellular events that occur during the processes of adhesion and spreading are spatio-temporal cytoskeletal rearrangements including the formation of actin fiber and its supramolecular organized "stress fiber," and of focal adhesion complex or adhesion plaques at the cellular basal side interacting with the extracellular matrix.[5]

Recent studies showed that the complex scenario of adhesion, spreading, and migration is conducted by the Rho family of small guanosine triphosphatase (GTPase), which includes Rho, Rac1, and Cdc42.[6,7] These proteins have essential roles in the regulation of the diverse cellular activities described above, and function as molecular switches in cellular signaling pathways, many of which influence cell morphology and motility. As schematically shown in Figure 1, upon receiving signals from plasma membrane receptors, these proteins are activated to trigger a variety of intracellular responses, including cytoskeletal organization, membrane trafficking, cell adhesion, migration, and polarity. A large focal adhesion complex

Correspondence to: T. Matsuda; e-mail: matsuda@med.kyushu-u.ac.jp

Contract grant sponsor: Organization for Pharmaceutical Safety and Research (OPSR) Promotion of Fundamental Studies in Health Science; contract grant number: 97-15
Contract grant sponsor: Ministry of Education, Culture, Sports, Science, and Technology of Japan Grant-in-Aid for Scientific Research; contract grant numbers: A2-12358017, B2-12470277

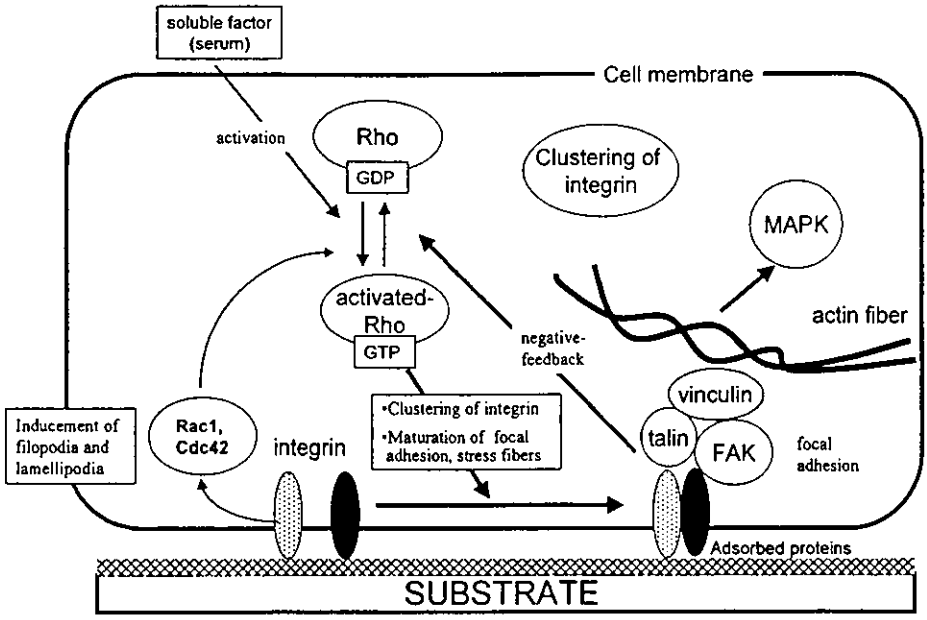

Figure 1. Proposed model for the regulation of Rho by both soluble factor and extracellular matrix. Cell adhesion via integrin/extracellular matrix coupling activates Rho family via the transmembrane signaling pathway, leading to the clustering of integrins and formation of focal adhesions, which also generate signals to down-regulate Rho, thereby preventing the excessive formation of focal adhesions. The spatio-temporal cytoskeletal organization via the assembled adhesional machinery influences cell shape and morphology. FAK, focal adhesion kinase.

forms as integrins are clustered, and proteins such as vinculin and talin are recruited to form an adhesion machinery. The Rho family and the integrins are intimately related at multiple levels.[8] Rho family activation leads to the assembly of actin-myosin filaments (stress fibers) and of associated focal adhesion complexes.[9,10] Rho cycles between a guanosine diphosphatase (GDP)-bound inactive state and a GTP-bound active state, thus operating via positive and negative feedback mechanisms (see Fig. 1). When Rac1 is activated, actin polymerization is induced and focal adhesion complexes form as integrins become clustered to produce lamellipodia[11] and membrane ruffles[12] as described below. When Cdc42 is activated, bundles of actin filaments protrude from the cell body in filopodia[13,14] or peripheral actin microspikes.[15] Figure 2 shows typical cell morphology as observed by atomic force microscopy and the fluorescence-labeled cytoskeleton of adhered cells with lamellipodia and filopodia. Cell morphology changes induced by Rho, Rac1, and Cdc42 activation share many aspects such as an apparent increase in polymerized actin, clustering of integrins, and assembly of large protein complexes containing vinculin, talin, focal adhesion kinase, and paxillin (Fig. 1).[16,17]

In this article, the substrate dependence of time-dependent cellular behaviors, such as changes in macroscopic cell shape and microscopic cell morphology, cytoskeletal dynamics, and cell motility, and the activation of Rho family in Swiss 3T3 fibroblasts, which were mainly used in biochemical studies on the Rho family during the first 24 h after cell plating, are discussed in conjunction with temporal activation and deactivation of these Rho families.

MATERIALS AND METHODS

Materials

Tissue culture polystyrene (TCPS) dishes (430165, Corning, NY), suspension culture polystyrene (PS) dishes (430588, Corning), and poly(ethylene terephthalate) (PET) film (SANPLATEC Co., Ltd., Osaka, Japan) were used for cell culture study. The PET film was cut into 100-mm-diameter discs, rinsed with phosphate-buffered saline (PBS), and placed in a 100-mm-diameter tissue culture plate.

Cell culture

Swiss 3T3 cells were commercially obtained from Dainippon Pharmaceutical Co., Ltd. (Osaka, Japan), and were cultured in Dulbecco's modified Eagle's medium (DMEM) (Gibco BRL, Grand Island, NY) containing 10% fetal calf serum (FCS) (Gibco), 2 m*M* L-glutamine, 100 U/mL penicillin, and 100 μg/mL streptomycin at 37°C, 98% humidity, and 5% CO_2. Before seeding, cells at confluence were incubated in DMEM without serum overnight in order to make

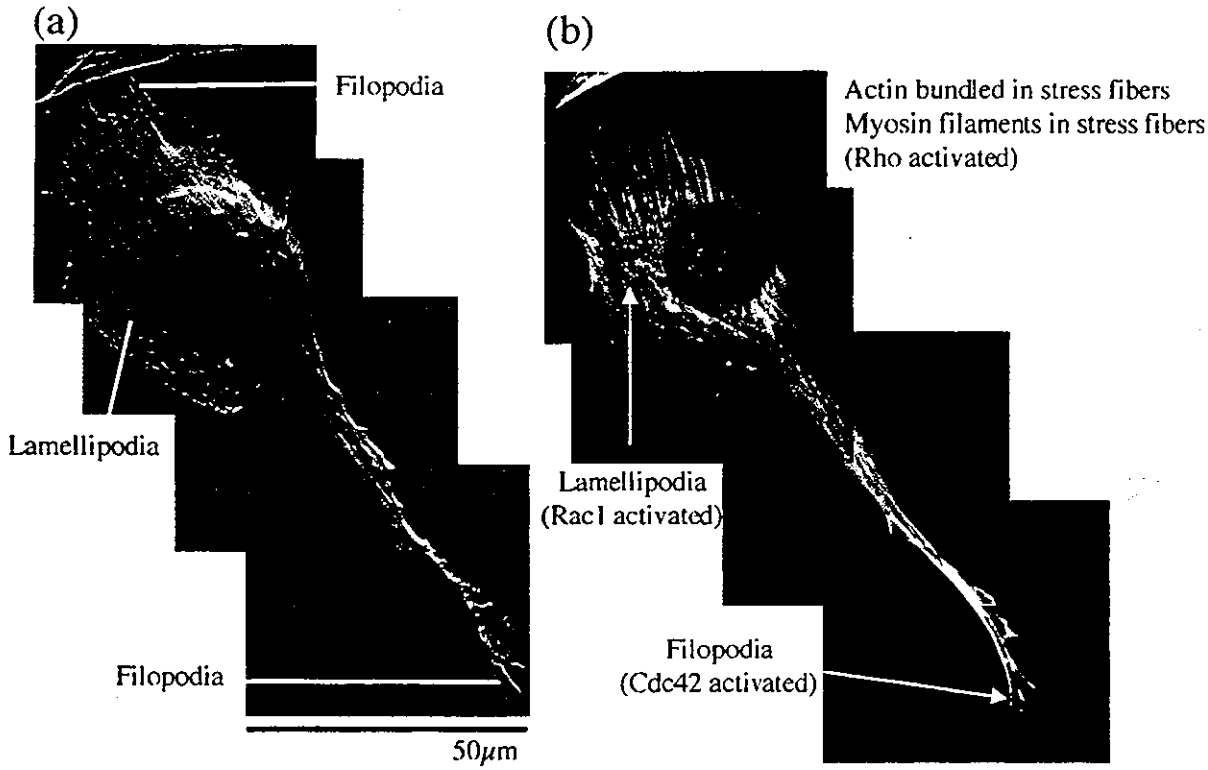

Figure 2. Morphology of lamellipodia and filopodia in a Swiss 3T3 cell adhered to TCPS. Rho activation leads to the assembly of actin-myosin filaments (stress fibers) and of associated focal adhesion complexes. Rac1 activation leads to the assembly of a meshwork of actin filaments at the cell periphery to the lamellipodia and membrane ruffling. Cdc42 activation induces the formation of actin-rich surface protrusions called filopodia. (a) Atomic force microscopy deflection mode image, and (b) fluorescence image of actin cytoskeleton.

them fall into the same cell cycle, GO. The cells were seeded at a density of 2×10^4 cells/cm^2 on respective dishes. The cells were incubated in 10% FCS-containing DMEM medium under the same conditions mentioned above for predetermined period: 0.5, 1, 3, 6, and 24 h.

Immunofluorescence microscopy

Cells were fixed in 10% formalin for 10 min, permeabilized in 0.5% Triton X-100 at room temperature for 5 min, and blocked with 1% bovine serum albumin (BSA) in PBS. The cells were incubated with anti-vinculin monoclonal antibody (at 1:100 dilution; Upstate Biotechnology, NY) in PBS for 1 h at room temperature. After a brief wash with PBS, they were further incubated with a secondary antibody (fluorescein isocyanate–anti-mouse immunoglobulin G at 1:100 dilution; KPL Inc., Gaithersburg, MD) plus rhodamine-phalloidin (at 1:100 dilution; Molecular Probes, Inc., Eugene, OR) in PBS for 1 h at room temperature. Images were acquired using a Bio-Rad Radiance 2000 confocal laser scanning microscopic system (Bio-Rad, Richmond, CA).

Affinity precipitation of Rho, Rac1, and Cdc42

The adhered cells were washed with PBS three times and lysed in RIPA buffer (10 m*M* Tris-HCl, 150 m*M* NaCl, 1% Triton X-100, 0.1% sodium dodecyl sulfate, 1 m*M* ethylenediaminetetraacetic acid, pH 7.4) containing protease and phosphatase inhibitors at the following final concentrations: 1 μg/mL leupeptin, 1 μg/mL aprotinin, 1 μg/mL pepstatin, 1 m*M* sodium orthovanadate, and 1 m*M* phenylmethylsulfonyl fluoride. Cell lysates were centrifuged at 1000*g* at 4°C for 10 min and the supernatant was transferred to a fresh tube. Protein concentration was determined by means of the BCA protein assay kit (Pierce, Rockford, IL) with BSA as the standard. Rho activity was determined by the affinity-precipitation method.[18] To determine the activation of Rho, 500 μg of protein (1 μg/μL cell lysate) was incubated with agarose beads conjugated GST-Rho binding domain (RBD) (Upstate Biotechnology) (20 μg) at 4°C for 60 min. The beads were washed three times with cold PBS and boiled in sample buffer. Bound Rho protein was detected by Western blotting using a monoclonal antibody as described below. The amount of RBD-bound Rho was normalized to the total amount of Rho in whole cell lysates for the comparison of Rho activity (level of GTP-bound Rho) in different samples. Values represent Rho activity relative to that of cells at time 0. That is, the time-dependent Rho, Rac1, Cdc42 activities were normalized to those of suspension cells, which were subjected to the serum-starved, staged cells and detached from the dishes before cell seeding. This method did not determine activation of the subset population of the Rho subfamily (Rho-A, -B, and -C). According to the manufacturer's instruction, this method allows precipitation of the

TABLE I
Parameters Characterizing the Movement of 3T3 Cells for 3–5 h and 23–25 h Culture on TCPS, PS, and PET

Parameter	Time (h)	TCPS	PS	PET
Total length of cell trajectory (μm)[a]	3–5	175.39 ± 27.01	200.35 ± 25.53	171.69 ± 15.28
	23–25	189.78 ± 38.34	227.92 ± 31.45	213.36 ± 71.15
Average speed of cell movement (μm/min)[b]	3–5	1.46 ± 0.23	1.67 ± 0.21	1.43 ± 0.13
	23–25	1.58 ± 0.32	1.90 ± 0.26	1.78 ± 0.59
Length of final cell displacement (μm)[c]	3–5	16.55 ± 13.39	30.29 ± 9.90	8.22 ± .
	23–25	27.86 ± 26.82	36.76 ± 26.87	24.39 ± 15.89
Average rate of cell displacement (μm/min)[d]	3–5	0.14 ± 0.11	0.25 ± 0.08	0.07 ± 0.03
	23–25	0.23 ± 0.22	0.31 ± 0.22	0.20 ± 0.12
Coefficient of dislocation efficiency[e]	3–5	0.10 ± 0.09	0.15 ± 0.05	0.05 ± 0.02
	23–25	0.14 ± 0.11	0.16 ± 0.10	0.12 ± 0.07

Values are given as the means ± SD.
[a]Total length of cell trajectory in every 2-min step.
[b]Average speed of cell locomotion defined as total length of cell trajectory/time of recording.
[c]Total length of final cell displacement of the cell from (i.e., distance between) the first and last points of the cell track.
[d]Average speed of cell locomotion defined as total length of cell displacement/time of recording.
[e]The ratio of cell displacement length to cell trajectory length. Coefficient of dislocation efficiency would equal 1 for the cell moving persistently along one straight line in one direction and zero for a random movement.

GTP-Rho (activated) not GDP-Rho (inactivated) at the detection limit of 0.5–2 μg/mL of detected Rho in lysates from the cells. To determine the activation of Rac1 and Cdc42, GST-p21 binding domain (PBD) conjugated agarose beads (Upstate Biotechnology) (10 μg) were used and the Western blotting technique as mentioned below was used. Results are given as means ± standard deviation (SD) of five runs.

Western blotting

Western blots of Cdc42 and Rho were separately run using the respective antibodies. The identification of bands detected was performed using the antibodies included in the commercial kits used. The proteins were separated in 10% sodium dodecyl sulfate polyacrylamide gel and transferred to the polyvinylidene difluoride membrane (Bio-Rad). The membranes were blocked in T-PBS (0.1% Tween 20 with PBS) with 1% BSA. After washing in PBS, the blots were incubated with the primary antibody (1 μg/mL in T-PBS): Rho (Santa Cruz Biotechnology Inc.), Rac1 (Upstate Biotechnology), or Cdc42 (Santa Cruz Biotechnology Inc.) antibody, at room temperature for 1 h. After washing with PBS, the blots were treated with the secondary antibody (1 μg/mL in T-PBS) (fluorescein isocyanate–anti-mouse immunoglobulin G; KPL Inc.) at room temperature for 1 h. Densitometry was performed using the Molecular Imager FX (Bio-Rad). At every measurement, the control was set as the value at time 0, and the value at each measurement was normalized to that of control.

Time-lapse analysis of cell migration

The substrate-dependent migratory behavior of cells was monitored by a time-lapse image-capturing system (HIMAWARI; Library Inc., Tokyo, Japan) connected to a phase-contrast microscope (IX70; Olympus, Tokyo, Japan) with a temperature and humidity controllable cell chamber (MATS-CO2CHK; TOKAI HIT, Shizuoka, Japan). Before the time-lapse recording experiment, cells were seeded at a density of 2×10^3 cells/cm^2 on each substrate and cultured with DMEM containing 10% FCS under 5% CO_2 for 3 or 23 h. Then, DMEM was exchanged with L15 (Gibco BRL) containing 10% FCS. This medium exchange was performed to adapt the cultured cells to the long observation period without needing to regulate CO_2 concentration in our cell chamber. Images of cells were captured every 2 min for 120 min. The coordinates of 10 isolated cells were measured by digitizing software using the position of their nuclei. The migratory track and the moving speed were calculated from the coordinates, and cell trajectories were presented in circular diagrams with the starting point of each trajectory situated in the diagram center. The parameters affecting cell motility were computed for each cell and are tabulated in Table I (definitions of parameters are given in the footnotes).

RESULTS

The adhesion and spreading states at 3 h and 24 h after plating were determined by fluorescence immunohistochemical staining and phase-contrast microscopy. The migratory potentials were time-lapse determined by measuring the time-lapse tracking of moving cells. The activation of Rho families (Rho, Rac1, and Cdc42) was determined by affinity precipitation and Western blotting techniques.

Cell adhesion and spreading

Swiss 3T3 fibroblasts, confluently grown and subjected to an overnight serum starvation before use,

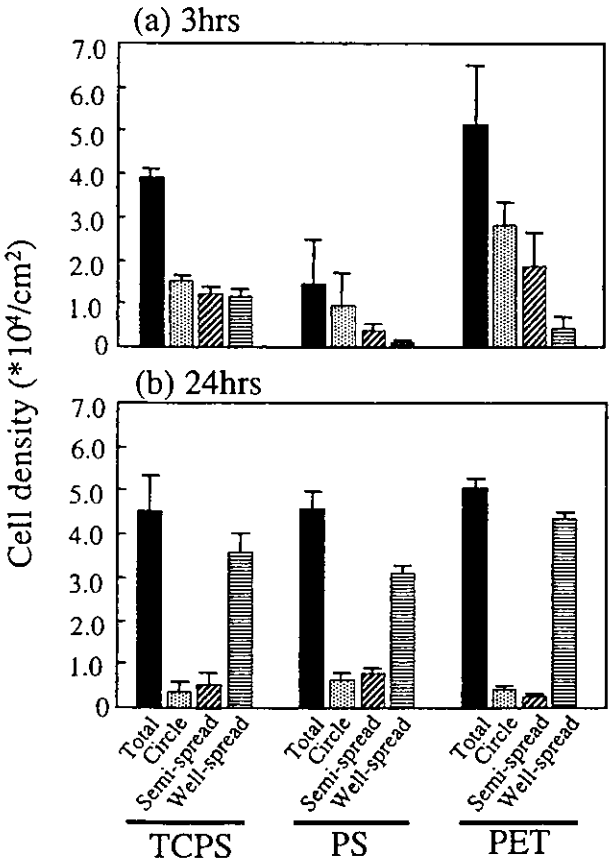

Figure 3. Number of adhered cells and subpopulation of cell shape (nonspread circular shape, semispread, and well-spread) on TCPS, PS, and PET at 3 h and 24 h after plating. At least 300 cells were analyzed at each time point.

were seeded and cultured on three different substrates (TCPS dishes, biological PS culture dishes, and PET film) in the serum-containing medium for up to 24 h. TCPS and PET substrates were selected as substrate characteristics of high cell adhesion and spreading, whereas biological PS was selected as a substrate characteristic of a markedly reduced adhesion and spreading.

The number of cells adhering to these substrates and the cell shape were determined under a phase-contrast microscope at 3 h and 24 h after plating. At 3 h, the number of adhered cells was the highest for PET, followed by that for TCPS, whereas a markedly reduced cell number was noted for PS, which was almost one-fourth to one-third of those on the former two substrates [Fig. 3(a)]. However, there was a marked difference in the spreading state between the three substrates: when cell shapes were roughly divided into three shapes such as circular (or round), semispread, and well spread, cells cultured on TCPS had almost equal subpopulations of these three different shapes. However, for the PET substrate, more than half (55%) of the cells remained round, approximately one-third (37%) had the semispread shape, and a very small population (<10%) had the well-spread shape. A higher subpopulation of round cells (approximately 71%) was found for PS. At 24 h after plating, there was little difference between the subpopulations of cells on TCPS and those on PET [Fig. 3(b)]. Most cells (80–86%) were well spread, and round ones remained <10%. Although the subpopulation of round cells adhering to PS was similar to those on TCPS and PET, the cells comprised <20% of the total populations. These cells were all living ones, which was confirmed by the trypan blue staining method.

Figure 4 shows the substrate-dependent relative occurrence of lamellipodia to total adhered cells. At 3 h, irrespective of type of the substrate, lamellipodia was found in 25–30% of the total cell population. At 24 h, an increased population of lamellipodia was noted in cells grown on all the substrates. Approximately 50–55% of adhered cells on TCPS and PET exhibited noticeable lamellipodia, whereas the subpopulation of cells with lamellipodia on PS remained around 40%.

Cytoskeletal dynamics

The cytoskeletal dynamics of actin stress fiber and vinculin in cells were determined by immunofluorescence microscopy using rhodamine-phalloidin to label α-actin and actin stress fibers, and anti-vinculin antibody to determine focal adhesion or adhesion plaques. Figures 5–7 show the time courses of the formation and distribution of focal adhesion and stress fibers in cells that adhered to these substrates. At 0.5–1 h after plating, regardless of the type of substrate, round cells

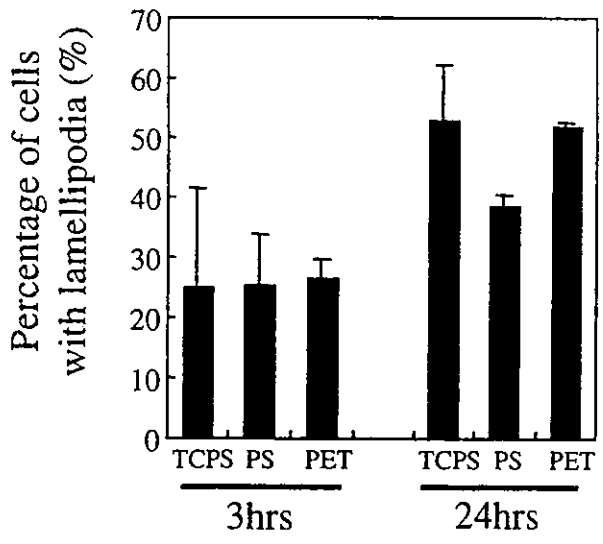

Figure 4. Substrate-dependent population of cells with lamellipodia at 3 h and 24 h after serum-starved cells were plated at a density of 2×10^4 cells/cm^2.

without any signs of spreading were dominant. Vinculin and α-actin were localized at the peripheral regions of adhered cells to form rings. At 3 h, the spreading state depended on the type of substrate: on TCPS, well-spread cells, which comprised almost one-third of the entire population, had actin fibers being developed to form stress fibers and vinculin localized at the front edges of spread cells (Fig. 5). These became more enhanced at 6 h after plating: stress fibers developed to transverse the intracellular space although major actin fibers were still localized at the peripheral regions of cells. Vinculin was distributed in spots at the front edges of peripheral regions as well as the central parts of intracellular regions.

However, on both PS and PET, cells at 3 h after plating did not exhibit any signs of spreading: a large population of round cells was noted (Figs. 6 and 7). At 6 h, the population of spread cells increased on PET, whereas nonspread cells were still dominant on PS. At 24 h after plating, irrespective of the type of substrate, cells were well spread on the substrates and developed prominent focal adhesions that were detected by vinculin staining: many stress fibers terminated at focal adhesions. The cell shapes of lamellipodia and filopodia were observed in these cells.

Cell migration

Cell migration was measured during 3–5 h and 23–25 h after plating. The positions of cells, which were sparsely seeded to reduce the probability of contact with each other, were acquired with a phase-contrast microscope, and images were taken at 2-min intervals during a total observation period of 120 min. Migratory tracks were determined from the positions of cell nuclei digitized on the images at a time interval from which the migration speed was calculated. The following parameters characterizing cell migration were computed for each cell: (a) the total length of cell trajectory, (b) the average speed of cell locomotion defined as the total length of cell trajectory/recording time, (c) the total length of the final displacement of the cell from (i.e., distance between) the first and last points of the cell track, (d) the average speed of cell locomotion defined as total length of cell displacement/time of recording, and (d) the cell displacement length to cell trajectory length, which is also called the coefficient of dislocation efficiency.[19,20] Table I lists these parameters obtained on the three substrates at the periods of 3–5 h and 23–25 h after plating.

Figure 8 shows examples of the migratory tracks (trajectories) of cells on the three substrate surfaces. During the first observation period (3–5 h), random migration of cells was observed on TCPS: cells exhibited membrane ruffling and moved via very frequent cycles of a large extent of expansion and retraction of pseudopods. The moving speed of the cells, calculated from the cell trajectory, was approximately 1.46 μm/min. In contrast, the cells that adhered to PS, on which cells were not spread well, moved by changing cell shape: cells exhibited very frequent cycles of a small extent of expansion and contraction of pseudopodia. The moving speed of the cells was 1.67 μm/min. The cells that adhered to PET appeared to remain at almost the same place: cells exhibited very slight expansion and contraction of pseudopodia at the same place. The moving speed of the cells was 1.43 μm/min. Although the total length of the cell trajectory was not strongly dependent on the type of substrate, both final displacement and the coefficient of dislocation efficiency were found to be the highest for PS, followed by TCPS and lastly, by PET.

However, during the well-spread period (23–25 h after plating), irrespective of type of substrate, the cells on all the substrates moved randomly, and the length of final displacement was considerably increased compared with that in the early period. The total length of the cell trajectory and the average cell migration speed were not significantly increased except for those for PET. On PS substrate, there was significant difference in parameters on cell motility between the early and late periods of observation. However, marked increases in the length of final displacement, the average rate of cell displacement, and the coefficient of dislocation efficiency were noted for both TCPS and PET substrates. These cell motility parameters for TCPS and PET became similar to those for PS at 24 h after plating.

Expressions of Rho, Rac1, and Cdc42

Time courses of Rho, Rac1, and Cdc42 activation during adhesion, spreading, and migration processes were determined by plating serum-starved cells onto each dish. The activities of Rho, Rac1, and Cdc42, determined by the affinity-precipitation method, were expressed as the amount of RBD-bound Rho normalized by the amount of Rho in whole-cell lysates. With the commercially available detection kit used here, only activated forms of the whole Rho subfamily (Rho-A, -B, and -C) were measured. Figure 9 shows the time course of Rho family activity of the cells adhered to the three different substrates. Values represent Rho activity relative to serum-starved cells on the dishes before cell seeding, at time 0. Regardless of the type of substrate, Rho activity increased with incubation time, reaching a maximal value (almost 1.5- to 2.0-fold higher than the basal level) at 0.5–1 h and gradually returning to the basal level at 24 h. This indicates that there is no significant difference in the

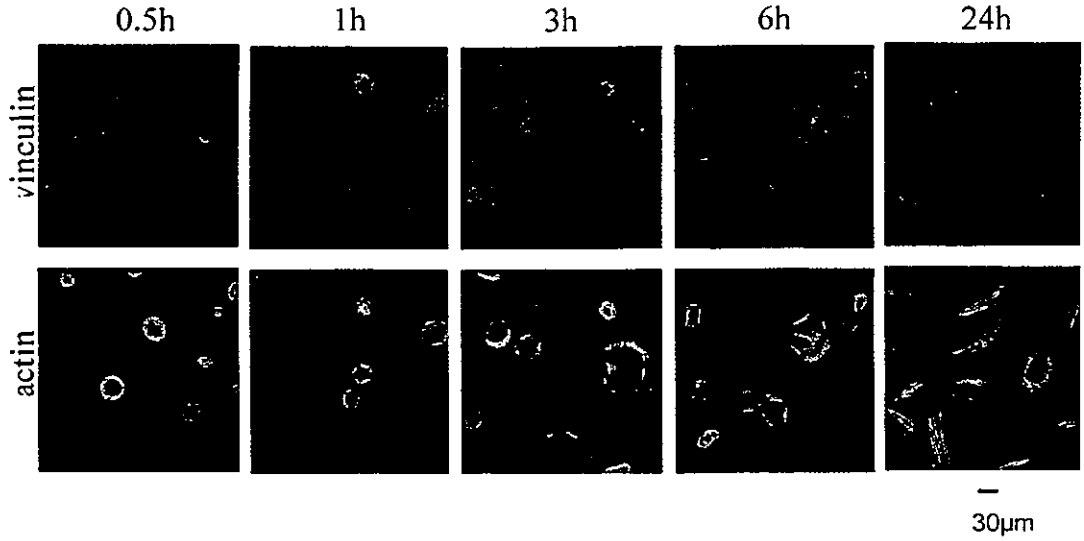

Figure 5.

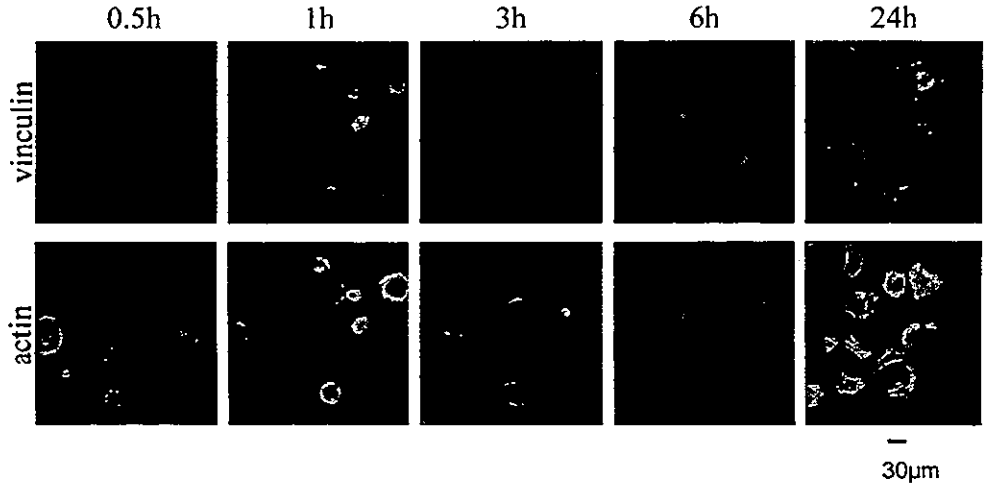

Figure 6.

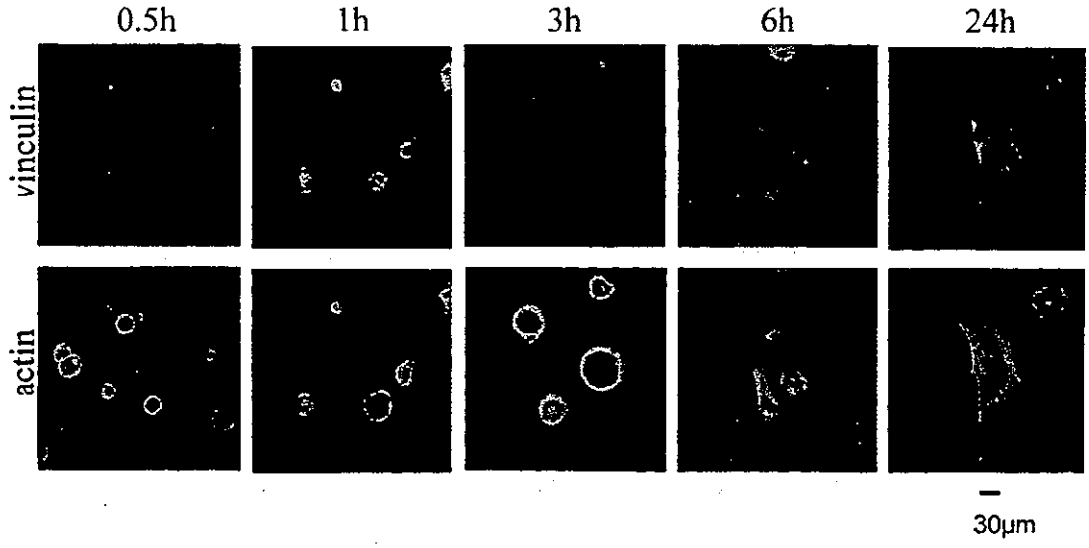

Figure 7.

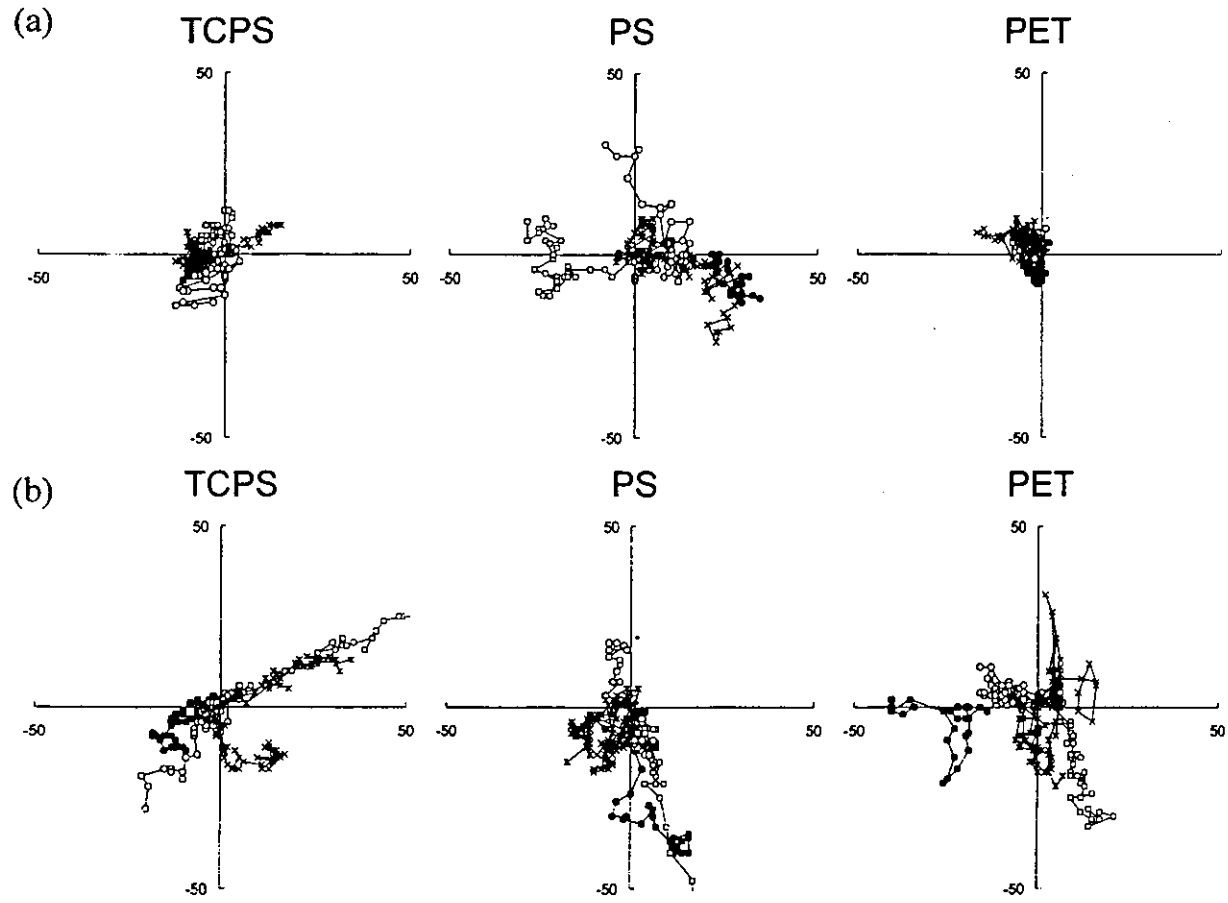

Figure 8. Migratory tracks of Swiss 3T3 cells on TCPS, PS, and PET drawn with the initial point of each trajectory being the origin of the plot. The images were recorded (a) 3–5 h, and (b) 23–25 h. After plating, and the positions of cell centroids were determined at 2-min intervals.

time course of Rho activation among the substrates. Rac1 activity of the cells adhering to TCPS and PET increased within a shorter time (0.5 h) and maintained the same level that was almost 1.4- to 1.5-fold higher than the control. In contrast, Rac1 activity of cells adhering to PS peaked at 0.5–1 h, and then returned to the basal level. Cdc42 activity of cells adhering to TCPS increased within a shorter time (0.5–1.0 h) and maintained the same level (approximately 1.5-fold higher than control) during the observation period. In contrast, Cdc42 activity of cells adhering to PS was very low and appeared to remain at the basal level, whereas that of cells adhering to PET increased within 0.5–1 h and maintained that level (1.2-fold higher than the basal level).

DISCUSSION

Tissue morphogenesis is driven by changes in cell shape, growth, and function that are coordinated in both time and space, and is governed by transmembrane signal transduction in the local tissue microenvironment

Figure 5. Time course of focal adhesion and stress fiber formation in cells adhered to TCPS. Cells were plated onto TCPS at a seeding density of 2×10^4 cells/cm^2. At the times indicated, cells were fixed and actin filaments were visualized with rhodamine-phalloidin, and in the same cells vinculin was localized by immunofluorescence microscopy using mouse anti-vinculin antibody to detect focal adhesions. Bar represents 30 μm.

Figure 6. Time course of focal adhesion and stress fiber formation in cells adhered to PS. The experimental procedure was the same as that in Figure 5.

Figure 7. Time course of focal adhesion and stress fiber formation in cells adhered to PET. The experimental procedure was the same as that in Figure 5.

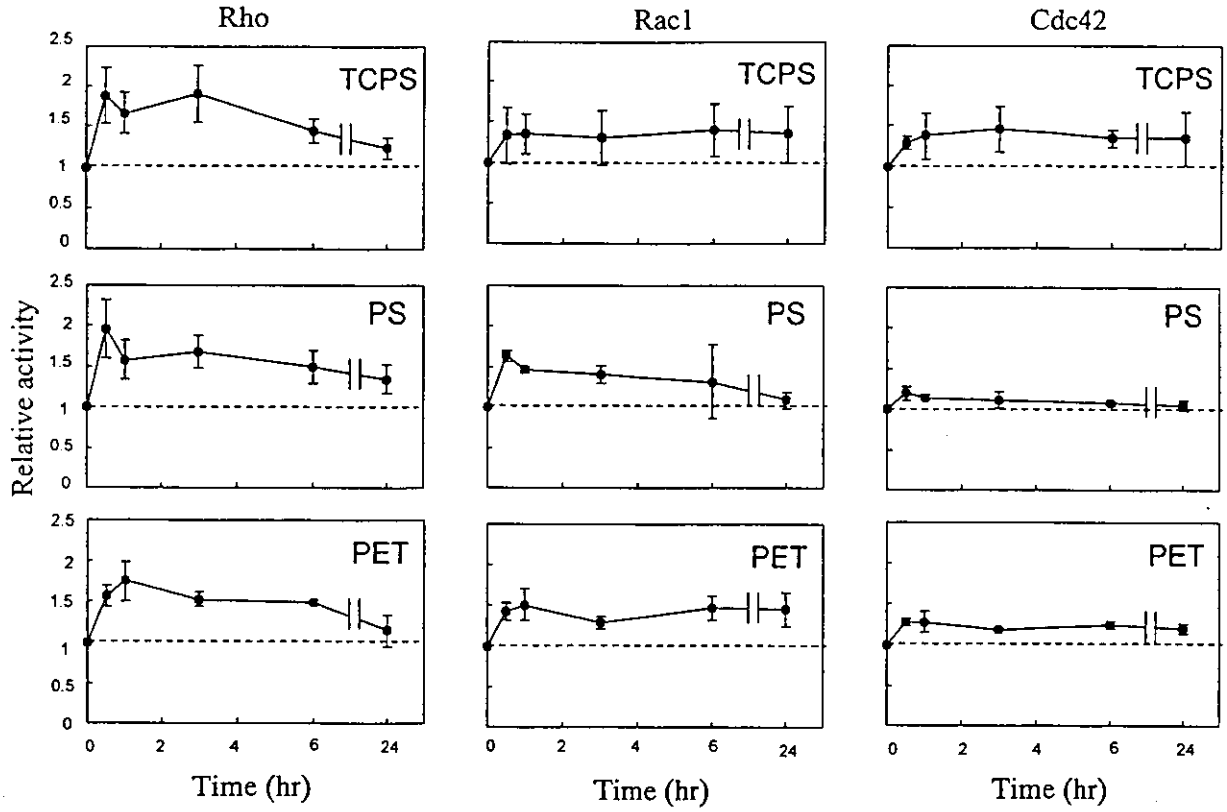

Figure 9. Relative activities of Rho GTPases (Rho, Rac1, and Cdc42) of cells adhering to TCPS, PS, and PET. Values represent corresponding Rho activity relative to serum-starved cells at time 0. Results are means ± SD from five experimental runs.

when stimulated by a variety of environmental cues.[21,22] As schematically shown in Scheme 1, integrin (cell receptor)-adhesive protein adsorbed to a synthetic substrate triggers transmembrane signaling, thereby activating Rho family and integrin clustering.{Scheme1} This induces cytoskeletal organization and the formation of an adhesion machinery as well as the deactivation of Rho (negative control).[23] These changes determine cell shape and morphology as well as cell migration.[24,25] Such sequential molecular events with positive and negative feedback and amplification occur.

In this study, the sequential events in the morphogenesis of cell-lined fibroblasts after plating for up to 24 h on three different substrates were determined. During the first 24 h after plating, various stages of cell behavior, such as macroscopic cell shape and microscopic morphology (lamellipodia and filopodia), cytoskeletal dynamics including stress fibers and adhe-

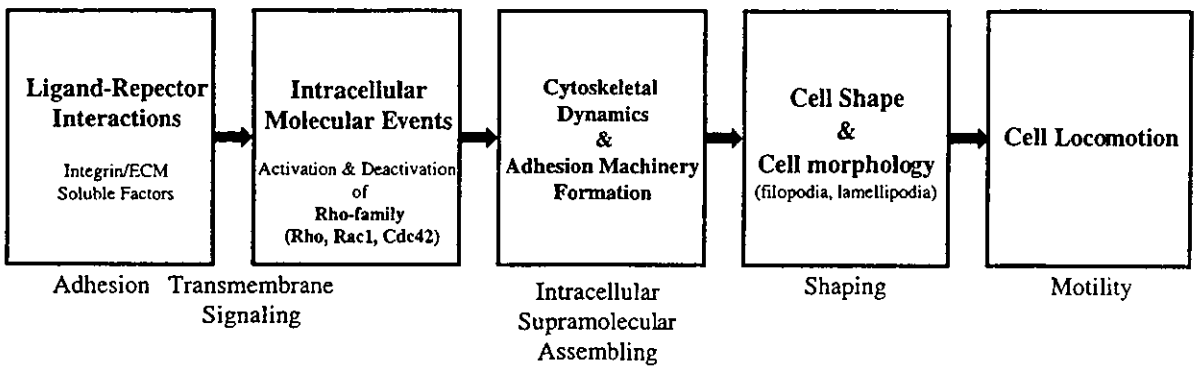

Scheme 1. Sequential molecular and cellular events during the adhesion and spreading processes. ECM, extracellular matrix.